Disorder effects on the ballistic transport of gated phosphorene superlattices

E. J. Guzmán,[1,*] O. Oubram,[1] O. Navarro,[2] and I. Rodríguez-Vargas[3,†]

[1]*Facultad de Ciencias Químicas e Ingeniería, Universidad Autónoma Del Estado de Morelos, Av. Universidad 1001, Col. Chamilpa, Cuernavaca, 62209 Morelos, México*

[2]*Unidad Morelia del Instituto de Investigaciones en Materiales, Universidad Nacional Autónoma de México, Antigua Carretera a Pátzcuaro No. 8701, Col. Ex Hacienda de San José de la Huerta, 58190 Morelia, Michoacán México*

[3]*Unidad Académica de Ciencia y Tecnología de la Luz y la Materia, Universidad Autónoma de Zacatecas, Circuito Marie Curie S/N, Parque de Ciencia y Tecnología QUANTUM Ciudad del Conocimiento, C.P. 98160 Zacatecas, México*

(Received 29 September 2022; revised 1 December 2022; accepted 15 December 2022; published 6 January 2023)

In this paper, we carry out a theoretical study of the electronic ballistic transport in gated phosphorene superlattices. Our work is focused on the effects by the random introduction of structural disorder in the electrostatic potential barriers. Specifically, we consider various degrees of disorder in the width and height of the barriers. To explain the transport of the charge carriers (electrons and holes) in the armchair direction of phosphorene, we employ a low-energy two-band Hamiltonian derived from the tight-binding model. The transmission and conductance are calculated by the transfer matrix technique and the Landauer-Büttiker formalism, respectively. We have found that both types of disorder affect the transmission and conductance in different ways, and we also found distinct effects on the charge carriers. In general, the disorder significantly reduces the transmission as well as the peak zones associated with the tunneling effect. Particularly, for disorder in the width, the transmission miniband structure is greatly degraded, while for disorder in the height, the miniband structure is preserved. The variation in the width of the barriers interferes directly with the Fabry-Pérot resonances of the propagating waves, while the variation in the height mainly reduces the magnitude of the transmission due to the dominance of evanescent waves. Consequently, the conductance loses its oscillatory characteristic and experiences flattening under the influence of disorder of the width, in contrast with the disorder of the height in which the oscillation prevails. Finally, we found that both types of disorder induce a redistribution of electron states. Specifically, the allowed energy bands are increased, and the occupation number as well as the accumulation of states are greatly reduced, which is in accordance with the effects of disorder observed in the transport properties.

DOI: 10.1103/PhysRevB.107.045407

I. INTRODUCTION

In recent years, a lot of research has been done on two-dimensional (2D) materials such as graphene and silicene, whose outstanding physical and electronic properties could be exploited to develop technological applications in nanoectronics. Phosphorene, another member in this class of 2D materials, is formed by phosphorus atoms distributed in a puckered honeycomb layer and linked by covalent bonds in sp^3 hybridization. In principle, the material known as black phosphorus (BP) has an orthorhombic crystal structure [1] and consists of layers of phosphorene stacked on top of each other and held together by weak van der Waals forces [2,3]. Analogously to graphene, phosphorene nanoflakes have been extracted from bulk BP by mechanical and electrochemical exfoliation in the laboratory [4–6]. In addition, other synthesis techniques [7] such as plasma-assisted etching [8,9], pulse laser deposition [10], and chemical vapor deposition [11] have been demonstrated. However, it has been found that phosphorus samples exhibit high oxidation during exposure to the environment and visible light [12,13]. To avoid this, several synthesis processes as well as aid substances to protect the phosphorene surface and provide long-term stabilization have been recently reported [14–21]. For instance, stability improvement has been found by covering phosphorene with layers of Al_xO_y [15,16], phosphorene fluorination induces antioxidation and antihydration effects [17,18], and phosphorene encapsulation with graphene and hexagonal boron nitride greatly reduces degradation [19–21]. Here, it is also relevant that the passivating substance minimally interferes with the phosphorene intrinsic electronic properties. Experimentally, it was discover that bulk BP is a semiconductor with an intrinsic bandgap of 0.31–0.35 eV at the high-symmetry Z point [22,23]. Later, using mathematical techniques such as the tight-binding model [24,25], the self-consistent pseudopotential method [26], and density functional theory (DFT) [27,28], the energy band structure of bulk BP was theoretically calculated. A substantial increase of the gap was discovered when BP is reduced by a few layers [27–29]. The single phosphorene layer is a semiconductor with moderate bandgap in the energy range 1.0–2.0 eV [24,28], with reference theoretical value of 1.5 eV at the Γ point [25,27]. Additionally, the energy band structure reveals high anisotropy between both directions of propagation (armchair and zigzag) as well as

*eric.guzman@uaem.edu.mx
†isaac@uaz.edu.mx

for both charge carriers (electrons and holes) [27,30,31]. In the Γ-*X* direction, corresponding to the armchair direction, the charge carriers follow Schrödinger (classic) physics, and in the Γ-*Y* direction, corresponding to zigzag, they follow Dirac (relativistic) physics. Even more, the band structure shows a marked difference in effective masses between the two directions, being heavier along the zigzag direction [31]. Also, phosphorene exhibits mobility for electrons of hundreds of $cm^2\ V^{-1}\ s^{-1}$, but the mobility for holes is higher, reaching up to 1000 $cm^2\ V^{-1}\ s^{-1}$ [32], which classifies phosphorene as a *p*-type semiconductor. The anisotropic characteristics of phosphorene are quite attractive from both the fundamental and technological standpoints. From the fundamental standpoint, the special characteristics of the charge carriers in the armchair and zigzag directions can give rise to exotic phenomena such as negative reflection and super-anti-Klein tunneling [33] as well as electronic cloaking of confined states [34]. From the technological standpoint, the anisotropic band structure of phosphorene opens the door to pseudospintronics [35], phosphorene being the only 2D material with this possibility so far. In addition, different investigators have documented the potential of phosphorene as a basis material in field effect transistors [36–38].

To take advantage of the intrinsic physical and electronic properties of 2D materials [39], different nanostructuring methods have been implemented for future electronics and optoelectronics applications [40–44]. Gated superlattices are quite attractive from the technological standpoint due to the possible modulability of the physical properties of 2D materials by simply applying an electrostatic potential through metallic gates. In the case of graphene, there are important breakthroughs in the fabrication of gated superlattices through the so-called dielectric patterning [45–50]. From the theoretical standpoint, there are extensive works about gated superlattices in the most relevant 2D materials; phosphorene is not the exception in this direction. In fact, the electronic, optical, and transport properties of phosphorene superlattices have been studied [51–57]. One factor that can have a considerable impact on the performance of gated superlattices is the unavoidable variation of height and width of the barriers or the so-called structural disorder. The impact of the structural disorder on the transport and transport-related properties in graphene and silicene superlattices has been documented [58–62]. For instance, Abedpour *et al.* [58] have investigated the effects of disorder on the width of the barriers in graphene superlattices. They show that the transmission and conductance are affected by the disorder strength of the width of the barriers. Esmailpour *et al.* [59] have studied stress-induced disorder in a graphene superlattice. They found that the conductance decreases with the increasing magnitude of strain disorder. Esmailpour *et al.* [60] also studied the effect of disorder associated with the velocity of charge carriers. They show that the kind and the strength of disorder affect the transmission and conductance of graphene superlattices. Regarding superlattices in silicene, Oubram *et al.* [61] have investigated the impact of structural disorder on transport and thermoelectric properties. They reported that these properties manifest a decrease as the intensity of the disorder increases. They found that a strong suppression of conductance, Seebeck coefficient, and power factor is induced by the structural disorder associated with the height of electrostatic barriers. Recently, Oubram *et al.* [62] have found a counterintuitive result that the structural disorder in magnetic silicene superlattices improves the magnetoresistance and the valley-spin polarization properties. Regarding phosphorene superlattices, reports addressing the impact of structural disorder are lacking. Thus, considering the relevance of phosphorene as a 2D material with remarkable intrinsic properties and the importance of gated superlattices as basis structures for nanoelectronic devices, we consider that a thorough assessment of the impact of structural disorder on the transport properties of phosphorene superlattices is needed.

In this paper, we carried out a theoretical study about the effects of structural disorder on the ballistic transport properties of gated phosphorene superlattices (GPSLs). The superlattice structure is formed by a series of electrostatic barriers of potential arranged along the armchair direction and oriented on the *x* axis. Specifically, the structural disorder that we consider is the variation of the width and height of the electrostatic barriers. For this purpose, this paper is presented as follows. Section II contains the tight-binding model theory in the low-energy range of phosphorene, where the four-band and subsequent two-band Hamiltonians are described [63]. Here, we describe our electronic device consisting of electrodes placed on a single layer of phosphorene, with the aim of studying the ballistic transport of the superlattices under the effect of disorder. To do this, we calculate the transmission probability using the transfer matrix technique and the conductance using the Landauer-Büttiker formalism [51]. The density of states (DOS) that complements our study is computed by the dispersion relation of the supercell wave vector. In Sec. III, the results obtained are presented. Here, we give the details of how the two types of disorder (width and height) are introduced as well as the full analysis and discussion of the transport properties under the effect of various degrees of disorder from weak to strong. In the last Sec. IV, the conclusions of our work are specified.

II. THEORETICAL MODEL

The theoretical fundamentals of the band structure and the electronic transport of the charge carriers in phosphorene have been well explained by the widely used tight-binding model [51,63], whose effective Hamiltonian in the momentum space is

$$H_{\mathbf{k}} = \sum_{\mathbf{k}} \widehat{c}^{\dagger}_{\mathbf{k}} \widehat{H}^{[4]}_{\mathbf{k}} \widehat{c}_{\mathbf{k}}, \tag{1}$$

where the four-vectors $\widehat{c}^{\dagger}_{\mathbf{k}} = (c^{\dagger}_{A\mathbf{k}} \quad c^{\dagger}_{B\mathbf{k}} \quad c^{\dagger}_{D\mathbf{k}} \quad c^{\dagger}_{C\mathbf{k}})$ and $\widehat{c}_{\mathbf{k}} = (c_{A\mathbf{k}} \quad c_{B\mathbf{k}} \quad c_{C\mathbf{k}} \quad c_{D\mathbf{k}})$ are the creation and annihilation operators, respectively, with the subscripts A, B, D, and C representing the four atoms in the unit cell of phosphorene (see Fig. 1).

The effective Hamiltonian $\widehat{H}^{[4]}_{\mathbf{k}}$ in the low-energy range around the symmetrical point Γ is given by

$$\widehat{H}^{[4]}_{\mathbf{k}} = \begin{pmatrix} \epsilon_A & H_{AB} & H_{AD} & H_{AC} \\ H_{BA} & \epsilon_B & H_{BD} & H_{BC} \\ H_{DA} & H_{DB} & \epsilon_D & H_{DC} \\ H_{CA} & H_{CB} & H_{CD} & \epsilon_C \end{pmatrix}, \tag{2}$$

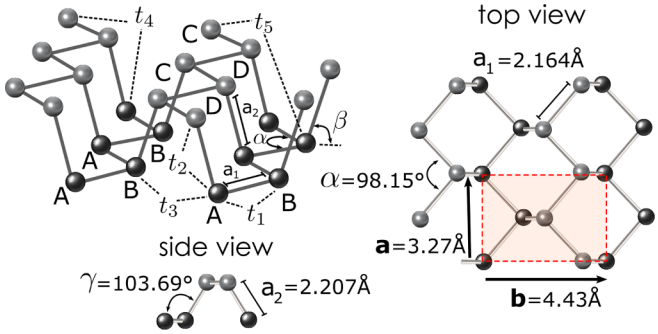

FIG. 1. Crystal structure of single-layer phosphorene. The interatomic distances, the hopping parameters (t_j), and the unit cell (red square) formed by 4 atoms of phosphorus (A–D) are shown.

with matrix elements obtained by the formula:

$$H_{j,l} = H^*_{l,j} = \sum_{\langle j,l\rangle} t_{j,l} \exp[i(\mathbf{r}_l - \mathbf{r}_j)\cdot\mathbf{k}], \tag{3}$$

where the sum runs over the first and second neighbor atoms l with respect to fixed atom j. The asterisk symbol (*) indicates the complex conjugate. Specifically, for phosphorene, we have

$$\begin{aligned} H_{AB} &= H_{DC} \\ &= 2\{t_1 \exp(-iR_1k_x) + t_3 \exp[i(R_1+2R_2)k_x]\} \\ &\quad \times \cos(R_0k_y), \\ H_{AD} &= H_{BC} = 4t_4 \cos[(R_1+R_2)k_x]\cos(R_0k_y), \end{aligned}$$

and

$$H_{AC} = H_{DB} = t_2 \exp(iR_2k_x) + t_5 \exp[-i(2R_1+R_2)k_x], \tag{4}$$

where the values of hopping integrals are $t_1 = -1.220$ eV, $t_2 = 3.665$ eV, $t_3 - 0.205$ eV, $t_4 = 0.105$ eV, and $t_5 = 0.055$ eV [25]. The interatomic distances projected on the x-y plane are $R_0 = a_1\sin(\alpha)$, $R_1 = a_1\cos(\alpha)$, and $R_2 = a_2\cos(\beta) = -a_2[\cos(\gamma)]/[\cos(\alpha/2)]$. In such expressions, the in-plane wave vector $\mathbf{k} = (k_x, k_y)$, and the lattice primitive vectors $\mathbf{a} = (a, 0)$ and $\mathbf{b} = (0, b)$ are specified.

Considering the symmetry (D_{2h} group) of the atomic lattice in phosphorene, the equivalence onsite energy between atoms $A(B)$ and $D(C)$, with the Fermi level taken as the zero-energy reference, the Hamiltonian can be simplified to the two-band model as follows:

$$\widehat{H}^{[2]}_{\mathbf{k}} = \begin{pmatrix} H_{AD} & H_{AB}+H_{AC} \\ H^*_{AB}+H^*_{AC} & H_{AD} \end{pmatrix} \equiv \begin{pmatrix} F_{\mathbf{k}} & G_{\mathbf{k}} \\ G^*_{\mathbf{k}} & F_{\mathbf{k}} \end{pmatrix}. \tag{5}$$

Diagonalizing this operator, that is, performing $\det|\widehat{H}^{[2]}_{\mathbf{k}} - \widehat{I}E_{\mathbf{k}}| = 0$, the energy spectrum yields

$$(E_{\mathbf{k}} - F_{\mathbf{k}})^2 - G^*_{\mathbf{k}}G_{\mathbf{k}} = 0, \tag{6}$$

or

$$E^{\pm}_{\mathbf{k}} = F_{\mathbf{k}} \pm \sqrt{G^*_{\mathbf{k}}G_{\mathbf{k}}}. \tag{7}$$

From this, we can derive the magnitude of the bandgap at the Γ point ($k_x = 0, k_y = 0$), which separates the valence and conduction bands by the magnitude:

$$\Delta = E^+_{\mathbf{k}=0} - E^-_{\mathbf{k}=0} = 4t_1 + 2t_2 + 4t_3 + 2t_5 = 1.54 \text{ eV}. \tag{8}$$

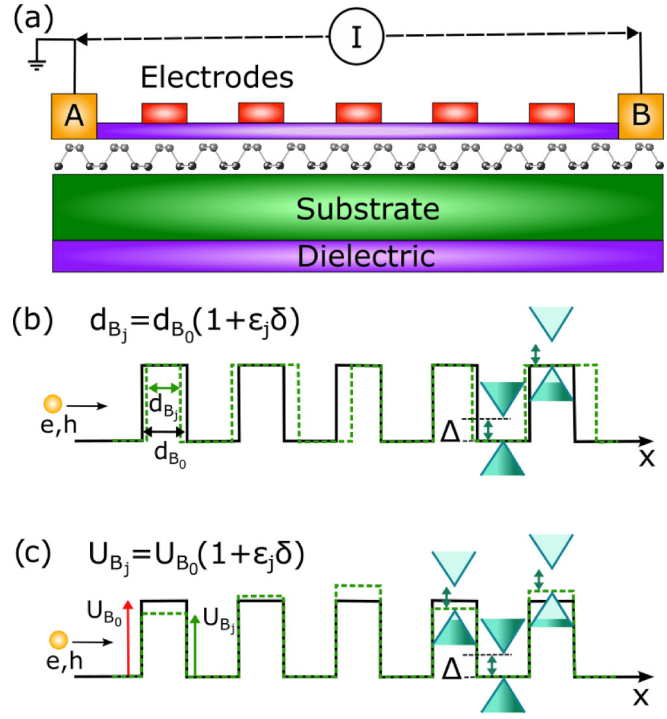

FIG. 2. (a) Possible electronic device based on gated phosphorene superlattices. The single layer of phosphorene is deposited on an isolated substrate and encapsulated between two protecting dielectric layers. Electrodes are installed as top gates that generate the electrostatic potential profile. (b) Effect of the structural disorder introduced in the width of the barriers on the superlattice profile. (c) Effect of the structural disorder introduced in the height of the barriers on the superlattice profile. The solid black lines represent the ordered superlattice profile, while the dashed green lines represent the disorder variation in each case.

In this paper, we theoretically study an electronic device made of phosphorene (see Fig. 2). To manipulate the electronic transport properties, a series of metallic electrodes are installed on top of the phosphorene layer, which is deposited on an insulating substrate. The electrodes generate a gated superlattice structure formed by N rectangular electrostatic barriers with potential or height U_B and width d_B, which are separated by zero potential regions or wells with distance d_W. The superlattice is arranged along the x axis that represents the armchair direction. Due to the presence of potential barriers, the cones at the γ point in the phosphorene band structure experience a shifting effect in energy and without changing the width of the gap (Δ). In addition, in Fig. 2, the Fermi energy level of the incident charge carriers is indicated on the cones so that the occupancy of states in the cones changes with respect of the height of the barriers.

The operator that includes the superlattice potential is given by

$$\widehat{H}_{\mathbf{k}} + U\widehat{I} = \begin{pmatrix} F_{\mathbf{k}}+U_j & G_{\mathbf{k}} \\ G^*_{\mathbf{k}} & F_{\mathbf{k}}+U_j \end{pmatrix}, \tag{9}$$

and whose dispersion relation is now

$$[(E_{\mathbf{k}} - U_j) - F_{\mathbf{k}}]^2 - G^*_{\mathbf{k}}G_{\mathbf{k}} = 0. \tag{10}$$

Here, the subscript j denotes either a barrier (B) region or a well (W) region.

The eigenfunction that solves the operator in Eq. (9) with its corresponding eigenvalue $E_{\mathbf{k}}$, associated with each region j, is expressed as

$$\psi_{\mathbf{k}}(\mathbf{r}) = \frac{1}{\sqrt{2}}\left[A_j\begin{pmatrix}1\\ \nu_j^+\end{pmatrix}\exp(ik_{x,j}x) + B_j\begin{pmatrix}1\\ \nu_j^-\end{pmatrix}\exp(-ik_{x,j}x)\right]\exp(ik_y y), \tag{11}$$

where $\mathbf{r} = (x, y)$, and the coefficients of the incident (+) and reflected (−) wave are defined as

$$\nu_j^{\pm} = \frac{G(\mp k_{x,j}, k_y)}{\lambda_j\sqrt{G_{\mathbf{k}}^* G_{\mathbf{k}}}}. \tag{12}$$

The factor $\lambda_j = \pm 1$ depends on if $(E_{\mathbf{k}} - U_j) > F_{\mathbf{k}}$ or $(E_{\mathbf{k}} - U_j) < F_{\mathbf{k}}$, respectively. According to Eqs. (4) and (5), it is easy to note that $G(\mp k_{x,j}, k_y) = G^*(\pm k_{x,j}, k_y)$.

Using the standard transfer matrix method, we can connect the unknown amplitudes of the incident and transmitted waves through the superlattice structure. Indeed, the input and output states that correspond to the semi-infinite left and right regions are related by the equation:

$$\begin{pmatrix}A_{\text{in}}\\ B_{\text{in}}\end{pmatrix} = M_T\begin{pmatrix}A_{\text{out}}\\ 0\end{pmatrix}, \tag{13}$$

where the total transfer matrix is detailed as follows:

$$M_T = D_0^{-1}\left(\prod_j D_j P_j D_j^{-1}\right)D_0, \tag{14}$$

with

$$D_j = \begin{pmatrix}1 & 1\\ \nu_j^+ & \nu_j^-\end{pmatrix}, \tag{15}$$

and

$$P_j = \begin{bmatrix}\exp(ik_{x,j}d_j) & 0\\ 0 & \exp(-ik_{x,j}d_j)\end{bmatrix}, \tag{16}$$

which are called the dynamic and propagation matrices, respectively. Here, d_j symbolizes the width of the barriers and wells ($j = B, W$). According to Eq. (10), the component $k_{x,j}$ admits a real or imaginary solution depending on the energy $E_{\mathbf{k}}$, transverse component k_y, and height U_j of the barrier. In the case of real component $k_{x,j}$, the physical meaning is a propagating wave inside of the barrier, while the imaginary case represents an evanescent wave.

Now we can calculate the ballistic transport properties of GPSLs. First, it is possible to estimate the transmission probability of the charge carriers by

$$\mathbb{T}(E, k_y) = \frac{1}{|M_{T(1,1)}|^2}. \tag{17}$$

Then under the Landauer-Büttiker formalism, the conductance is calculated as the integral of the transmission for all transverse channels of the component k_y, namely,

$$\mathbb{G}(E) = G_0\int_{-k_y^{\max}}^{k_y^{\max}}\mathbb{T}(E, k_y)dk_y, \tag{18}$$

where $G_0 = e^2 L_y/\hbar$, and L_y is the transverse length of the phosphorene layer. The limit of the integration $k_y^{\max}$ symbolizes the maximum value of the transverse component (k_y) in which the propagation in the x direction vanishes ($k_x = 0$).

Finally, the DOS associated with the superlattice structure is given by

$$\text{DOS}(E) = \frac{1}{2\pi}\left|\frac{\partial q_{\text{SL}}}{\partial E}\right|, \tag{19}$$

where q_{SL} is the supercell wave vector. In fact, the DOS complements our study and offers a better understanding of the transport properties of GPSLs.

III. RESULTS

In this section, we present a theoretical study of the effects of structural disorder on the ballistic transport in GPSLs. We analyze how the disorder of the superlattice affects the transmission and conductance of charge carriers in the valence and conduction bands. Specifically, the type of disorder that we introduce is related to the size of the width as well as in the height of the electrostatic barriers.

First of all, we consider an ordered superlattice structure formed by $N = 5$ barriers with potential or height $U_0 = 0.15$ eV, width $d_{B_0} = 4$ nm, and separated by wells of width $d_W = 12$ nm. This structure serves as the basis for our model. Then we introduce a certain degree of disorder using the following mathematical expressions:

$$d_{B_j} = d_{B_0}(1 + \varepsilon_j\delta), \tag{20}$$

and

$$U_{B_j} = U_0(1 + \varepsilon_j\delta), \tag{21}$$

where δ is the degree or percentage of disorder, and ε_j in the range $[-1, 1]$ represents a random number that modifies each barrier (B_j) independently. In our calculations, we consider both weak (0–20%) and strong (30–50%) disorder. An ordered superlattice corresponds to the case without disorder (0%). The methodology that we follow generates a large number (>100) of random superlattice profiles for each disorder percentage. Then we numerically calculate the average of the transmission and conductance of all profiles. As we know, 100 is the number of profiles where this calculation stabilizes and the changes in the average are negligible; however, in this paper, we choose a number of 200 profiles to ensure better accuracy.

First, we analyze the transport properties for the case of disorder in the width (d_{B_j}) of the barriers. For this, we consider 200 superlattice profiles where the widths of the 5 barriers are randomly generated using Eq. (20) in each profile independently. Specifically, the variation of the width directly affects the exponential factor within the propagating matrix [Eq. (16)].

In Fig. 3, we show a color map of the transmission probability ($\mathbb{T}$) as a function of the Fermi energy (E_{F}) and the wave vector component k_y. Here, several degrees of disorder—both weak: (a) 0% (b) 5%, (c) 10%, and (d) 20%; and strong: (e) 30% and (f) 50%—have been considered. The value of transmission probability is measured from 0 (blue color) indicating total reflection to 1 (dark red color) indicating perfect

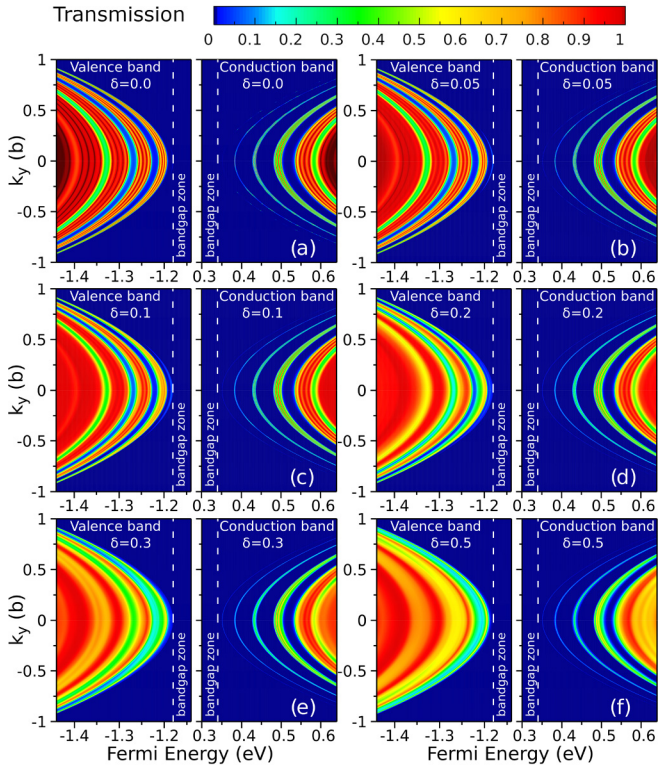

FIG. 3. Transmission probability ($\mathbb{T}$) as a function of Fermi energy (E_F) and transversal wave vector component (k_y) for a superlattice of 5 barriers of potential or height $U = 0.15$ eV and width $d_B = 4$ nm, for different degrees of disorder (0, 5, 10, 20, 30, and 50%) in the width of the barriers. The transmission is appreciated below the top of the valence band ($E_F < -1.18$ eV) and above the bottom of the conduction band ($E_F > 0.34$ eV). The same energy interval is considered in all figures.

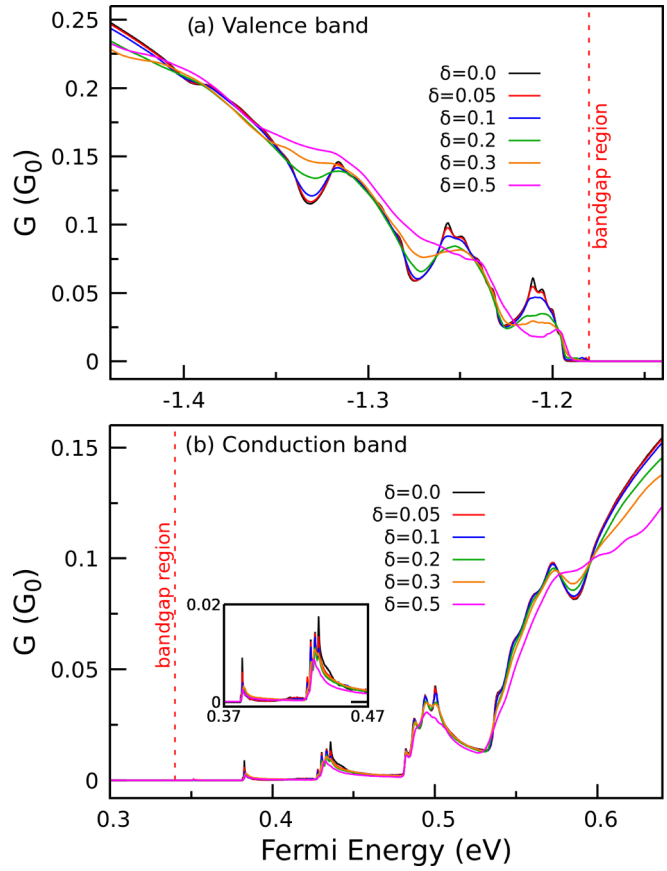

FIG. 4. Conductance ($\mathbb{G}$) as a function of Fermi energy (E_F) for a superlattice of 5 barriers of height $U = 0.15$ eV and width $d_B = 4$ nm, for different degrees of disorder in the width (0, 5, 10, 20, 30, and 50%). The conductance is shown for (a) the valence band and (b) the conduction band.

transmission associated with the tunnel effect phenomenon. The transmission in each disorder case is shown both for the valence and conduction bands located below and above the Fermi level $E_F = 0$, respectively. The energy bands are separated by a bandgap with magnitude of 1.52 eV [see Eq. (8)], whose limits are found at -1.18 and 0.34 eV, indicated by vertical dashed lines. It is very important to mention that, according to scientific reports [25], the energy range of validity of the tight-binding theory in phosphorene is ∼0.3 eV below and above the bandgap; therefore, we have adapted to that fact in our calculations and analysis.

As we can see in Fig. 3(a), the ordered case shows high-transmission zones called minibands colored in red, which are alternated with low-transmission zones called minigaps colored in blue. Inside the minibands, there are very marked peak zones that achieve perfect transmission ($\mathbb{T} = 1$) as a consequence of the tunnel effect. Additionally, we note that the valence band is formed by larger minibands in contrast to the conduction band, which can be explained by the implicit nature of phosphorene as a *p*-type semiconductor.

Now as the disorder degree increases, the transmission minibands are significantly reduced. At the same time, the transmission minigaps are slightly increased. Also, we observe that the reduction effect is stronger in the valence band than in the conduction band. For weak disorder (5%), the structure of the minibands with the tunnel peaks is still preserved. However, for greater disorder, the miniband structure is rapidly degraded since the borders of the minibands are expanded and vanished due to the narrowing of the minigaps. Additionally, it is notable that the tunnel peaks are completely lost above disorder of 10%. This is because the tunnel channels are strongly linked to the width of the barriers and wells, so the disorder interferes directly with the Fabry-Pérot resonances. In fact, here, in the case of GPSLs, Fabry-Pérot resonances take place at normal incidence, contrary to gated graphene superlattices in which Klein tunneling determines the electron transmission at normal incidence [64,65]. Here, it is also important to mention that Fabry-Pérot resonances can arise in practically all angular range of GPSLs, in contrast to gated graphene superlattices in which collimation effects shape the transmission properties at near normal incidence [64,66]. In this context, it is expected that structural disorder has a greater impact on the Fabry-Pérot resonances of GPSLs and consequently on their corresponding transport properties. In general, the average of the transmission of all superlattice profiles leads to a smoothing effect over the entire energy range for both bands. However, we must highlight that disorder has a greater impact in the valence band in contrast to the conduction band.

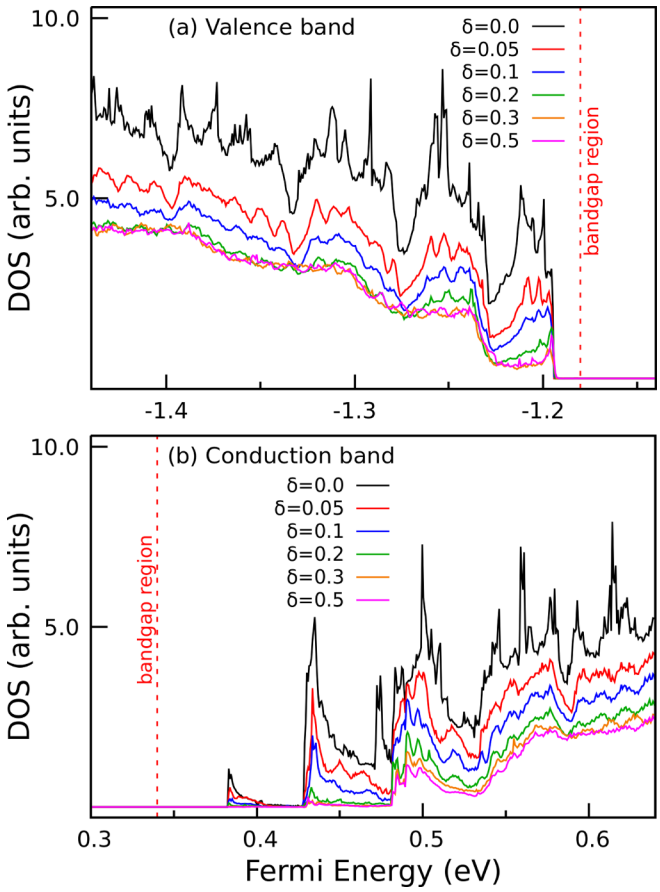

FIG. 5. Density of states (DOS) as a function of Fermi energy (E_F) for a superlattice of 5 barriers of height $U = 0.15$ eV and width $d_B = 4$ nm, for different degrees of disorder in the width of the barriers (0, 5, 10, 20, 30, and 50%). The DOS of (a) the valence band and (b) the conduction band are appreciated.

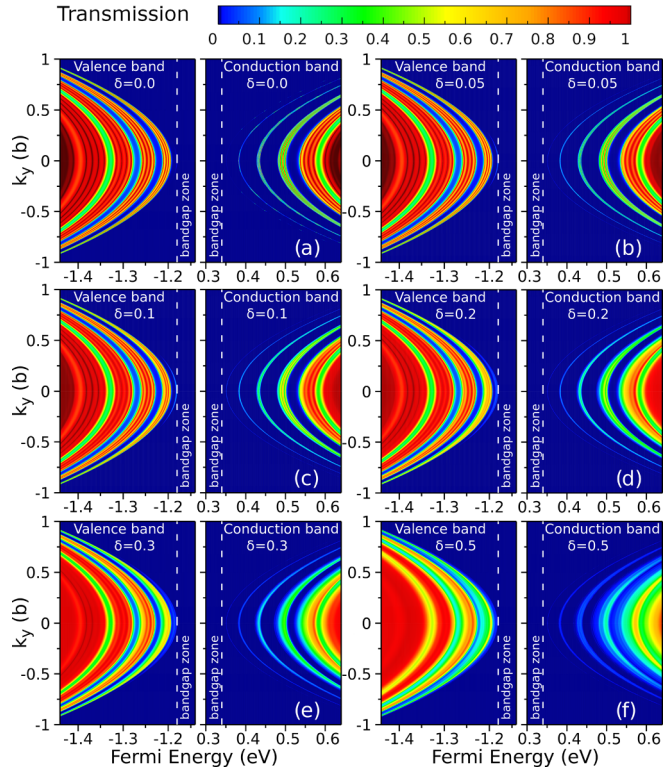

FIG. 6. Transmission probability ($\mathbb{T}$) as a function of Fermi energy (E_F) and transversal wave vector component (k_y) for a superlattice of 5 barriers of height $U = 0.15$ eV and width $d_B = 4$ nm, for different degrees of disorder: (a) 0%, (b) 5%, (c) 10%, (d) 20%, (e) 30%, and (f) 50% in the height of the barriers. The transmission is appreciated below the top of the valence band ($E_F < -1.18$ eV) and above the bottom of the conduction band ($E_F > 0.34$ eV). The same energy interval is considered in all figures.

In Fig. 4, we show the conductance ($\mathbb{G}$) as a function of the Fermi energy for degrees of disorder of 0, 5, 10, 20, 30, and 50%. Conductance is calculated directly from the results of the transmission (Fig. 3) using the Landauer-Büttiker formula in Eq. (18). The energy range includes (a) the valence band and (b) the conduction band, which allows us to study the conductance of holes and electrons through GPSLs. As we note, for ordered superlattice (0%), the conductance curve shows a very marked oscillatory behavior. In addition, at the low-energy range near the gap, the conductance exhibits peaks or drastic changes, which result from the fine miniband structure of the transmission. On the other hand, at large energies for both holes and electrons far from the gap, the conductance loses its oscillatory property, its behavior curve becomes flat, and the peaks are drastically reduced. This is due to the fact that the transmission increases and the minibands become wider. It is important to highlight that the conductance of the valence band is higher than the one corresponding to the conduction band; in contrast, the peaks in the conduction band are more pronounced.

Now as we increase the degree of disorder, the conductance gradually losses the oscillations as well as the peaks. The averaging process of the random profiles leads to a flattening effect in the conductance. It is evident that the effects of disorder have more impact in the valence band than the conduction band. Furthermore, an important fact is that, for weak disorder (5–20%), the conductance that corresponds to the conduction band still maintains the qualitative oscillating trend shown by the ordered superlattice (0%), which is an aspect to consider in the possible manufacture of electronic devices for this type of nanostructures with possible disorder.

To end this first analysis, in Fig. 5, we show the DOS as a function of Fermi energy (E_F) for different degrees of disorder in the width of the barriers, which we have previously considered. The DOS shows the allowed energy levels in (a) the valence band and (b) the conduction band, as well as the occupation number for holes and electrons in each band, respectively. As we can see in Fig. 5, for the ordered superlattice case (0%), the DOS shows that the occupancy number of charge carriers that contributes in the transport is the largest. Then as the degree of disorder increases, the DOS gradually decreases. This is consistent with the fact that the probability of transmission is reduced by the introduction of the disorder. In addition, the peaks of high accumulation of the DOS also disappear. Hence, the charge carriers are redistributed and moved to occupy other energy levels where the occupation number is low, balancing the DOS in both bands. The redistribution of the DOS is an important characteristic observed in

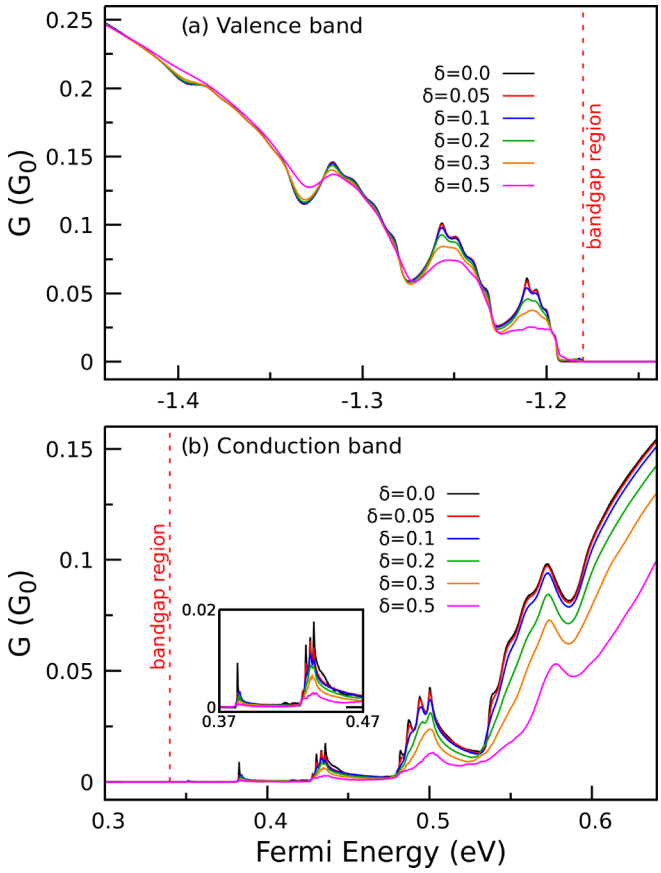

FIG. 7. Conductance ($\mathbb{G}$) as a function of Fermi energy (E_F) for a superlattice of 5 barriers of height $U = 0.15$ eV and width $d_B = 4$ nm, for different degrees of disorder in the height (0, 5, 10, 20, 30, and 50%). The conductance is shown for (a) the valence band and (b) the conduction band.

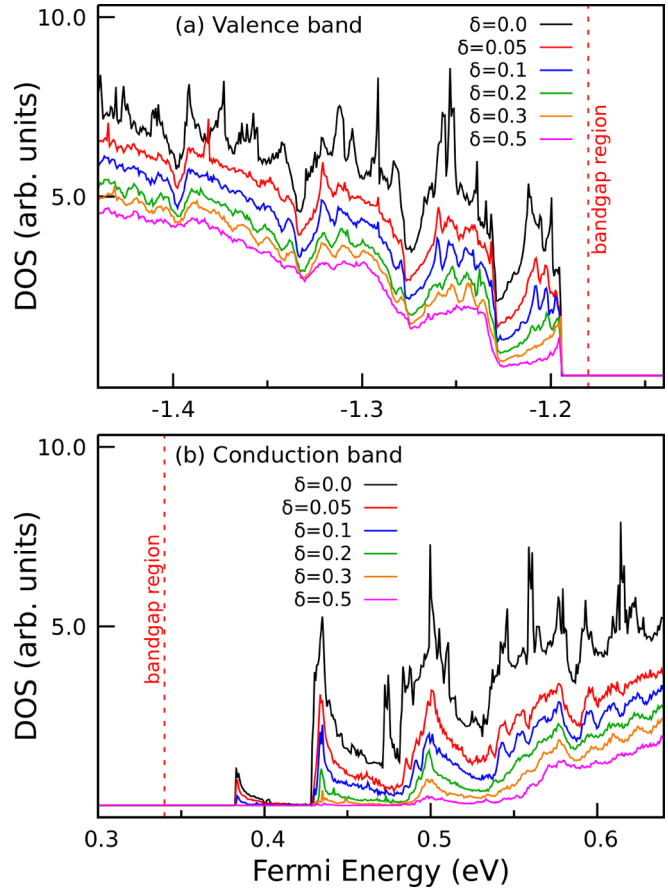

FIG. 8. Density of states (DOS) as a function of Fermi energy (E_F) for a superlattice of 5 barriers of height $U = 0.15$ eV and width $d_B = 4$ nm, for different degrees of disorder in the height of the barriers (0, 5, 10, 20, 30, and 50%). The DOS of (a) the valence band and (b) the conduction band are appreciated.

this class of low-dimensional materials, which is used to study different phenomena and electronic applications.

The second case that we analyze is the disorder in the height of the electrostatic barriers. We carry out an analogous procedure considering 200 superlattice profiles where the height of the 5 barriers is randomly generated using Eq. (21) in each profile independently. Specifically, for each potential generated, it is numerically required to solve the dispersion relation given in Eq. (10) to obtain the component $k_{x,j}$.

Figure 6 shows a map of the transmission ($\mathbb{T}$) as a function of Fermi energy (E_F) and the transverse component (k_y). Again, the degrees of disorder that we introduce are 0, 5, 10, 20, 30, and 50% in the height of the barrier. Also, in each disorder case are visualized the valence and conduction bands in an energy range of 0.34 eV above and below the bandgap. For the ordered superlattice (0%), the transmission exhibits a well-defined miniband structure. In addition, we can appreciate peak zones with $\mathbb{T} = 1$ (dark red) indicating a perfect transmission associated with the tunnel effect phenomenon as well as zones with $\mathbb{T} = 0$ (blue) indicating a total reflection.

As the degree of disorder increases, the transmission in both bands considerably decreases. The conduction band is very affected for this type of disorder (see Fig. 6). The miniband structure is stable and maintains both well-defined shape and borders until 20% degree of disorder. Also, the peak zones of the tunnel effect are still observed until this degree of disorder. For strong disorder (>30%), the miniband structure disappears since its borders are wider and the minigaps are narrower. This is because the height of the barriers have more relevance in the evanescent waves; hence, the disorder directly affects the magnitude of the transmission. In general, a smoothing effect of the transmission between minibands and minigaps throughout the energy range considered in this paper (0.34 eV around the gap) is appreciated. We emphasize that the disorder has a stronger impact on the transmission of the conduction band than the valence band, as confirmed below with the conductance calculation.

Figure 7 shows the conductance ($\mathbb{G}$) as a function of Fermi energy (E_F), for weak (0, 5, 10, and 20%) and strong (30 and 50%) disorder in the height of the barriers for both (a) the valence band and (b) the conduction band. The conductance is derived from the transmission (Fig. 6) using Eq. (18). As we can see, in the case of the ordered superlattice (0%), the conductance shows an oscillatory behavior in both bands, that is, high-conductance zones alternated with low-conductance zones. Also, we can appreciate peaks or drastic changes in the conductance. Then as the disorder of the height increases, the

conductance greatly decreases in both bands. The reduction of magnitude of the conductance is gradual but maintaining its qualitative oscillatory trend. For high disorder, the curve is flattening. Hence, the oscillatory behavior, even with the presence of disorder, is an important aspect to consider at the moment of fabrication of electric devices using this type of nanostructures.

Finally, the DOS as a function of Fermi energy (E_F) for the distinct degrees of disorder introduced in the height of the barriers is shown in Fig. 8. The DOS shows the allowed energy levels and the occupation number for (a) holes in the valence band and (b) electrons in the conduction band. For the ordered superlattice case (0%), the DOS shows the largest occupancy number of carriers contributing to the electronic transport. Then as the disorder gradually increases, the occupation decreases. This is in agreement with the reduction in transmission and conductance observed previously. It is important to mention that, qualitatively, the effect is like the one found in the DOS of the disorder in the width of barriers (Fig. 5). However, quantitatively, the disorder related to the width of the barriers has more impact in the DOS of the valence band than the disorder of the height of the barriers. For the conduction band, the impact of both disorders in the DOS is reverted. In addition, the high accumulation peaks of the DOS are also strongly affected. In this case, the redistribution of the states is only perceived for strong disorder. In fact, the charge carriers are redistributed, populating energy levels with low DOS. These results provide a better vision and understanding of how disorder affects the transport properties of GPSLs.

IV. CONCLUSIONS

In summary, we show that structural disorder has a strong effect on the ballistic transport of GPSLs. We have considered two types of disorder: first, a disorder in the width of the electrostatic barriers and, second, a disorder in the height of the barriers. In both cases, various degrees of disorder—both weak and strong—were analyzed, and the results obtained were compared with the ordered case. We have found that each type of disorder has a different influence on the transport properties as well as different impacts depending on the charge carriers. For the case of the width, as the disorder increases, the transmission is reduced rapidly, leading to a smoothing effect between minibands and minigaps. Additionally, the miniband structure is more degraded in the valence band than the conduction band. The peaks associated with the tunneling effect disappear above a disorder of 5% since the width variation directly affects the Fabry-Pérot resonances in the barrier energy region. Consequently, the conductance is reduced and loses its characteristic oscillatory behavior, flattening as the disorder increases. Here, the impact is much greater in the valence band than in the conduction band. For the case of the height, as the disorder grows, the transmission decays considerably. However, the miniband structure as well as the tunneling peaks are still preserved up to a disorder of 20% since the height variation mainly affects the magnitude of the transmission. The conductance is reduced in both bands but maintains its characteristic oscillatory shape, which is lost with strong disorder. Finally, both types of disorder redistribute the DOS. The peaks of high accumulation of DOS associated with the energy minibands of the ordered case are significantly reduced as the disorder increases.

ACKNOWLEDGMENTS

E.J.G thanks CONACYT-Mexico for the Postdoctoral Research Fellowship. I.R.-V. would like to acknowledge CONACYT-Mexico for the financial support through Grant No. A1-S-11655.

[1] R. Hultgren, N. S. Gingrich, and B. E. Warren, J. Chem. Phys. **3**, 351 (1935).
[2] L. Pauling and M. Simonetta, J. Chem. Phys. **20**, 29 (1952).
[3] Y. Du, C. Ouyang, S. Shi, and M. Lei, J. Appl. Phys. **107**, 093718 (2010).
[4] A. Castellanos-Gomez, L. Vicarelli, E. Prada, J. O. Island, K. L. Narasimha-Acharya, S. I. Blanter, D. J. Groenendijk, M. Buscema, G. A. Steele, J. V. Alvarez *et al.*, 2D Mater. **1**, 025001 (2014).
[5] J. Li, C. Chen, S. Liu, J. Lu, W. P. Goh, H. Fang, Z. Qiu, B. Tian, Z. Chen, and C. Yao, Chem. Mater. **30**, 2742 (2018);
[6] M. B. Erande, M. S. Pawar, and D. J. Late, ACS Appl. Mater. Interfaces **8**, 11548 (2016).
[7] S. C. Dhanabalan, J. S. Ponraj, Z. Guo, S. Li, Q. Bao, and H. Zhang, Adv. Sci. **4**, 1600305 (2017).
[8] J. Jia, S. K. Jang, S. Lai, J. Xu, Y. J. Choi, J. H. Park, and S. Lee, ACS Nano **9**, 8729 (2015).
[9] W. Lu, H. Nan, J. Hong, Y. Chen, C. Zhu, Z. Liang, X. Ma, Z. Ni, C. Jin, and Z. Zhang, Nano Res. **7**, 853 (2014).
[10] Z. Yang, J. Hao, S. Yuan, S. Lin, H. M. Yau, J. Dai, and S. P. Lau, Adv. Mater. **27**, 3748 (2015).
[11] J. B. Smith, D. Hagaman, and H. F. Ji, Nanotechnology **27**, 215602 (2016).
[12] J. O. Island, G. A. Steele, H. S. van der Zant, and A. Castellanos-Gomez, 2D Mater. **2**, 011002 (2015).
[13] A. Ziletti, A. Carvalho, D. K. Campbell, D. F. Coker, and A. H. Castro Neto, Phys. Rev. Lett. **114**, 046801 (2015).
[14] D. K. Sang, H. Wang, Z. Guo, N. Xie, and H. Zhang, Adv. Funct. Mater. **29**, 1903419 (2019).
[15] R. Galceran, E. Gaufres, A. Loiseau, M. Piquemal-Banci, F. Godel, A. Vecchiola, O. Bezencenet, M.-B. Martin, B. Servet, F. Petroff *et al.*, Appl. Phys. Lett. **111**, 243101 (2017).
[16] X. Luo, Y. Rahbarihagh, J. C. M. Hwang, H. Liu, Y. Du, and P. D. Ye, IEEE Electron Device Lett. **35**, 1314 (2014).
[17] X. Tang, W. Liang, J. Zhao, Z. Li, M. Qiu, T. Fan, C. S. Luo, Y. Zhou, Y. Li, Z. Guo *et al.*, Small **13**, 1702739 (2017).
[18] X. Tang, H. Chen, J. S. Ponraj, S. C. Dhanabalan, Q. Xiao, D. Fan, and H. Zhang, Adv. Sci. **5**, 1800420 (2018).
[19] R. A. Doganov, E. C. T. O'Farrell, S. P. Koenig, Y. Yeo, A. Ziletti, A. Carvalho, D. K. Campbell, D. F. Coker, K. Watanabe, T. Taniguchi *et al.*, Nat. Commun. **6**, 6647 (2015).

[20] X. Chen, Y. Wu, Z. Wu, Y. Han, S. Xu, L. Wang, W. Ye, T. Han, Y. He, Y. Cai *et al.*, Nat. Commun. **6**, 7315 (2015).

[21] A. Avsar, I. J. Vera-Marun, J. Y. Tan, K. Watanabe, T. Taniguchi, A. H. CastroNeto, and B. Ozyilmaz, ACS Nano **9**, 4138 (2015).

[22] R. W. Keyes, Phys. Rev. **92**, 580 (1953).

[23] Y. Maruyama, S. Suzuki, K. Kobayashi, and S. Tanuma, Physica B+C **105**, 99 (1981).

[24] Y. Takao, H. Asahina, and A. Morita, J. Phys. Soc. Jpn. **50**, 3362 (1981).

[25] A. N. Rudenko and M. I. Katsnelson, Phys. Rev. B **89**, 201408(R) (2014).

[26] H. Asahina, K. Shindo, and A. Morita, J. Phys. Soc. Jpn. **51**, 1193 (1982).

[27] J. Qiao, X. Kong, Z.-X. Hu, F. Yang, and W. Ji, Nat. Commun. **5**, 4475 (2014).

[28] H. Liu, A. T. Neal, Z. Zhu, Z. Luo, X. Xu, D. Tománek, and P. D. Ye, ACS Nano **8**, 4033 (2014).

[29] S. Das, W. Zhang, M. Demarteau, A. Hoffmann, M. Dubey, and A. Roelofs, Nano Lett. **14**, 5733 (2014).

[30] A. Mishchenko, Y. Cao, G. L. Yu, C. R. Woods, R. V. Gorbachev, K. S. Novoselov, A. K. Geim, and L. S. Levitov, Nano Lett. **15**, 6991 (2015).

[31] C. J. Páez, K. DeLello, D. Le, A. L. C. Pereira, and E. R. Mucciolo, Phys. Rev. B **94**, 165419 (2016).

[32] F. Xia, H. Wang, and Y. Jia, Nat. Commun. **5**, 4458 (2014).

[33] Y. Betancur-Ocampo, F. Leyvraz, and T. Stegmann, Nano Lett. **19**, 7760 (2019).

[34] S. Molina-Valdovinos, K. J. Lamas-Martínez, J. A. Briones-Torres, and I. Rodríguez-Vargas, J. Phys.: Condens. Matter **34**, 195301 (2022).

[35] S. W. Jung, S. H. Ryu, W. J. Shin, Y. Sohn, M. Huh, R. J. Koch, C. Jozwiak, E. Rotenberg, A. Bostwick, and K. S. Kim, Nat. Mater. **19**, 277 (2020).

[36] M. Buscema, D. J. Groenendijk, S. I. Blanter, G. A. Steele, H. S. J. van der Zant, and A. Castellanos-Gomez, Nano Lett. **14**, 3347 (2014).

[37] L. Li, Y. Yu, G. J. Ye, Q. Ge, X. Ou, H. Wu, D. Feng, X. H. Chen, and Y. Zhang, Nat. Nanotechnol. **9**, 372 (2014).

[38] S. Das, M. Demarteau, and A. Roelofs, ACS Nano **8**, 11730 (2014).

[39] G. G. Naumis, Rev. Mex. Fis. **67**, 050102 (2021).

[40] S. Yan, X. Zhu, J. Dong, Y. Ding, and S. Xiao, Nanophotonics **9**, 1877 (2020).

[41] J. Yang, K. Kim, Y. Lee, K. Kim, W. C. Lee, and J. Park, FlatChem **5**, 50 (2017).

[42] E. Rani and L. S. Wong, Adv. Mater. Technol. **4**, 1900181 (2019).

[43] K. Shavanova, Y. Bakakina, I. Burkova, I. Shtepliuk, R. Viter, A. Ubelis, V. Beni, N. Starodub, R. Yakimova, and V. Khranovskyy, Sensors **16**, 223 (2016).

[44] M. Dragoman, A. Dinescu, D. Dragoman, and F. Comanescu, Nanotechnology **32**, 345203 (2021).

[45] C. Forsythe, X. Zhou, K. Watanabe, T. Taniguchi, A. Pasupathy, P. Moon, M. Koshino, P. Kim, and C. R. Dean, Nat. Nanotechnol. **13**, 566 (2018).

[46] S.-C. Chen, R. Kraft, R. Danneau, K. Richter, and M.-H. Liu, Commun. Phys. **3**, 71 (2020).

[47] R. Huber, M.-H. Liu, S.-C. Chen, M. Drienovsky, A. Sandner, K. Watanabe, T. Taniguchi, K. Richter, D. Weiss, and J. Eroms, Nano Lett. **20**, 8046 (2020).

[48] Y. Li, S. Dietrich, C. Forsythe, T. Taniguchi, K. Watanabe, P. Moon, and C. R. Dean, Nat. Nanotechnol. **16**, 525 (2021).

[49] Y. Xu, C. Horn, J. Zhu, Y. Tang, L. Ma, L. Li, S. Liu, K. Watanabe, T. Taniguchi, J. C. Hone *et al.*, Nat. Mater. **20**, 645 (2021).

[50] R. Huber, M.-N. Steffen, M. Drienovsky, A. Sandner, K. Watanabe, T. Taniguchi, D. Pfannkuche, D. Weiss, and J. Eroms, Nat. Commun. **13**, 2856 (2022).

[51] S. D. Sarkar, A. Agarwal, and K. Sengupta, J. Phys.: Condens. Matter **29**, 285601 (2017).

[52] M. Tahir and P. Vasilopoulos, J. Phys.: Condens. Matter **29**, 425302 (2017).

[53] X. J. Li, J. H. Yu, K. Luo, Z. H. Wu, and W. Yang, Nanotechnology **29**, 174001 (2018).

[54] X. Li, W. Yang, K. Luo, and Z. Wu, Nanotechnology **31**, 105205 (2020).

[55] W. Li and F. Cheng, Phys. E **114**, 113631 (2019).

[56] A. Boroughani and E. Faizabadi, Ann. Phys. **531**, 1900202 (2019).

[57] A. Boroughani and E. Faizabadi, Superlattices Microstruct. **151**, 106779 (2021).

[58] N. Abedpour, A. Esmailpour, R. Asgari, and M. R. R. Tabar, Phys. Rev. B **79**, 165412 (2009).

[59] A. Esmailpour, H. Meshkin, and M. Saadat, Phys. E **50**, 57 (2013).

[60] A. Esmailpour, H. Meshkin, and R. Asgari, Solid State Commun. **152**, 1896 (2012).

[61] O. Oubram, O. Navarro, E. J. Guzmán, and I. Rodríguez-Vargas, Phys. E **120**, 114100 (2020).

[62] O. Oubram, J. G. Rojas-Briseño, S. Molina-Valdovinos, and I. Rodríguez-Vargas, Phys. Rev. B **105**, 115408 (2022).

[63] M. Ezawa, New J. Phys. **16**, 115004 (2014).

[64] J. A. Briones-Torres, J. Madrigal-Melchor, J. C. Martínez-Orozco, and I. Rodríguez-Vargas, Superlattices Microstruct. **73**, 98 (2014).

[65] M. I. Katsnelson, K. S. Novoselov, and A. K. Geim, Nat. Phys. **2**, 620 (2006).

[66] P. E. Allain and J. N. Fuchs, Eur. Phys. J. B **83**, 301 (2011).